TRMM Radar Observations of Shallow Precipitation over the Tropical Oceans

DAVID A. SHORT AND KENJI NAKAMURA

Institute for Hydrospheric–Atmospheric Sciences, Nagoya University, Nagoya, Japan

(Manuscript received 14 October 1999, in final form 1 April 2000)

ABSTRACT

Observations from the precipitation radar aboard the Tropical Rainfall Measuring Mission satellite provide the first opportunity to map vertical structure properties of rain over the entire Tropics and subtropics. Storm height histograms reveal a distinct bimodal distribution over the oceans with the lowest mode near 2 km and the upper mode at 5 km. The low mode is the dominant feature over regions previously associated with precipitating marine stratocumulus/stratus and trade wind cumulus. In those regions a lognormal distribution fits the observed storm height distributions quite well, and a strong correlation exists between conditional mean rainfall rate and storm height. In addition, the low mode appears within the major tropical convergence zones associated with significant precipitation, and in those regions a mixed lognormal distribution is used to separate the storm height distribution into two parts: shallow and deep. In this exploratory analysis, the correlation between rainfall intensity and storm height is used in combination with the mixed lognormal distribution to estimate that shallow precipitation composes approximately 20% of the total precipitation over tropical oceans during both El Niño and La Niña conditions.

1. Introduction

Precipitation from shallow clouds over the tropical and subtropical oceans generally occurs in the form of light rain/drizzle from stratocumulus/stratus (Austin et al. 1995) and as showers from well-developed trade wind cumuli (Baker 1993). In an early analysis of coincident wind and rain observations recorded in ship logbooks during the mid-nineteenth century, Loomis (1882) determined that rain was a rare occurrence within the trade wind belts of the North and South Atlantic Ocean, being recorded in less than 2% of the entries. He noted that these regions of deficient rainfall were in marked contrast to the near-equatorial maximum found between the NE and SE trades. Loomis' remarkable contribution is consistent with Petty's (1995) comprehensive global analysis of late-twentieth-century ship observations of present weather. Petty focused on the qualitative reports of precipitation type and intensity in the Comprehensive Ocean–Atmosphere Data Set (COADS; Woodruff et al. 1987). Other studies of the COADS data have provided climatological patterns of the extensive trade wind cumulus and marine stratocumulus/stratus regimes (Warren et al. 1988), including their seasonal cycle (Klein and Hartmann 1993; Norris 1998b) and long-term variability (Bajuk and Leovy 1998a,b).

Petty (1999) combined later surface synoptic reports of precipitation with satellite infrared observations to determine the correspondence between the occurrence of rain and the presence of shallow clouds. He found that 20%–40% of the surface reports of nondrizzle precipitation over much of the ocean east of Australia, within view of Japan's Geostationary Meteorological Satellite (to about 170°W), were associated with warm cloud tops (infrared temperature $\geq$ 273 K). The sparse sampling of ship reports makes them suitable for investigations of climatological patterns and long-term variability in precipitating clouds. Satellites with passive sensors provide more frequent and more uniform coverage, at the cost of indirect observations of precipitation/cloud characteristics. However, calibration and validation of satellite rainfall retrieval algorithms ultimately depends on surface in situ measurements (Thiele 1988).

Visible, infrared, and microwave satellite data reveals contrasts between precipitating shallow marine clouds and the relatively uniform ocean background that can be exploited to provide estimates of vertically integrated liquid water and microphysical properties related to rainfall production (Han et al. 1994; Inoue 1987; Petty 1994; Kummerow et al. 1996). Liu et al. (1995) utilized infrared and microwave data over a large sector of the equatorial western Pacific Ocean to estimate that 14%

Corresponding author address: David A. Short, ENSCO, Inc., Suite 230, 1980 N. Atlantic Ave., Cocoa Beach, FL 32931.
E-mail: david.short@ensco.com

of all precipitating clouds had warm tops and that they contributed 4% of total rainfall. Their study region included portions of the intertropical convergence zone (ITCZ), the South Pacific convergence zone (SPCZ), and the trade wind belt north of the equator. Lin and Rossow (1997) used visible/infrared data from the International Satellite Cloud Climatology Project (ISCCP; Schiffer and Rossow 1983; Rossow and Schiffer 1991) in combination with microwave satellite observations to estimate that 10%–20% of the total precipitation over the oceans between 50°N and 50°S is produced by warm clouds. Lin et al. (1998) found warm cloud tops with effective cloud particle radii consistent with drizzle in 30% of cloudy conditions for matched Meteosat special sensor microwave imager observations over the North Atlantic Ocean in summer. While satellite observations offer a great advantage in terms of global coverage, there is some ambiguity in partitioning the liquid water content between precipitation and clouds in passive microwave retrievals (Wilheit 1986). In addition, visible/infrared data provide information from the tops of clouds, which can frequently obscure lower-precipitating clouds.

In regions where shallow marine boundary layer clouds are dominant, satellite data have provided detailed information on mesoscale variability, particularly open and closed cells (Houze 1993). Low-level convergence patterns and upward motion would be expected to favor precipitation formation in clouds at the edges (center) of open (closed) cells. Agee et al. (1973) reported that open cells preferably occur east of the continents over warm ocean currents, and closed cells preferably occur west of the continents over cooler ocean currents. Agee and Dowell (1974) combined satellite data with conventional rawinsonde observations to determine that the convective depth (height of the low-level temperature inversion) associated with open cells was 2.3 km, whereas that associated with closed cells was 1.3 km. Austin et al. (1996) found that rainband formation in the local convergence zone upwind of Hawaii was frequently associated with the arrival of cloud patches and lines originating in the undisturbed trade wind region far to the northwest of Hawaii, a region where closed cells predominate. They also identified a change in the rainband regime from contiguous to cellular and associated it with the evolution of synoptic-scale features far upwind of Hawaii.

Observation of precipitation within stratus/stratocumulus and trade wind cumulus cloud fields has been a prominent objective in numerous major field projects over the past four decades. The Warm Rain Project (Lavoie 1967), its predecessors, and successors have provided observations of trade wind cumulus clouds in the local convergence zone northeast of Hawaii (Smolarkiewicz et al. 1988) and in the undisturbed flow farther northeast. The Barbados Oceanographic and Meteorological Experiment (BOMEX) was conducted during disturbed and undisturbed conditions in the trade winds of the western Caribbean (Holland and Rasmussen 1973). The First ISCCP Regional Experiment (FIRE; Cox et al. 1987) focused primarily on the radiative and microphysical properties of marine stratus/stratocumulus, although important observations of precipitation were also made (Wang and Wang 1994; Austin et al. 1995). Dynamics of the physical processes associated with transitions from stratus/stratocumulus to trade wind cumulus were the subject of the recent Atlantic Stratocumulus Transition Experiment (ASTEX) field campaign (Albrecht et al. 1995; Bretherton et al. 1995). The Coupled Ocean–Atmosphere Response Experiment (COARE; Webster and Lukas 1992) was conducted over the warm pool of the western equatorial Pacific Ocean, providing measurements of precipitation and cloudiness over a wide variety of conditions, including those described as having trade wind characteristics (Johnson and Lin 1997). Johnson et al. (1996) showed that the height of the low-level stable layer (near 800 mb) in the COARE region was somewhat variable ($\pm$50 mb or $\pm$0.5 km), consistent with the variability observed in the height of the trade wind inversion in regions dominated by large-scale subsidence (Schubert et al. 1995). Yuter et al. (2000) found a strong positive correlation between sea surface temperature and inversion height in meridional transects of the marine stratocumulus region west of Baja, California, during the 1997 Pan American Climate Studies (PACS) Tropical Eastern Pacific Process Study (TEPPS).

Over the past several decades evidence has steadily increased of low-level trade wind–like inversions of temperature and humidity in regions identified as climatological zones of convergence, deep convection, and heavy precipitation. Merceret (1976) identified dry holes within the eastern Atlantic ITCZ. Ramage et al. (1981) reported that the trade wind inversion extended to the latitude of the central Pacific equatorial convergence zone without significant change along the trade wind trajectory. Firestone and Albrecht (1986) found a low-level inversion in 50% of dropwindsonde profiles from the central equatorial Pacific and reported little evidence to support the idea that the inversion height significantly increases toward the equator. Johnson et al. (1996) described low-level stable layers with trade wind–like structure over the equatorial western Pacific warm pool. The primary mechanisms for establishing and maintaining such inversions are a local balance between large-scale subsidence and upward fluxes of latent and sensible heat from buoyant plumes rising from the sea surface (Houze 1993). Advection of stable conditions by the trade winds (Schubert et al. 1995), radiative cooling at the top of low-level moist/cloudy layer and detrainment/subsidence at mid-levels from nearby convection (Mapes and Zuidema 1996) are also contributing mechanisms. Thus far the evidence of low-level inversions over the tropical oceans within regions of frequent deep convective activity and precipitation have been provided by surface and airborne observations of cloud-

iness, moisture, temperature, and wind. Shallow precipitating clouds have also been observed; however, quantitative estimates of their contribution to total rainfall are lacking. Views of these regions from satellite sensors are frequently obscured by the attendant widespread upper-level cloudiness, limiting observations of low-level cloudiness and shallow precipitation.

The first spaceborne precipitation radar (PR), an active microwave instrument aboard the Tropical Rainfall Measuring Mission (TRMM) satellite, was designed to measure rain and its vertical structure over the vast tropical oceans and continents. The PR's sensitivity has exceeded expectations, allowing routine detection of rainfall intensities as low as 0.5 mm h^{-1} (Kummerow et al. 1998). The PR operates at a wavelength of 2.2 cm, allowing penetration of even the heaviest obscuring cloud layers and detection of underlying precipitation. This, combined with a vertical resolution of 250 m, makes the PR an effective platform for investigating shallow precipitation. The PR functions somewhat as a global precipitation profiler (Gage et al. 1996) without Doppler capabilities, providing information on the vertical structure of rain. The PR is now well into its third year of operations, providing meteorologists with unprecedented observations of a wide variety of weather systems (see, e.g., Simpson et al. 1998), including the most recent El Niño–La Nina conditions over the Pacific Ocean (Morrissey 1998).

The purpose of this paper is to analyze storm height and rainfall-rate statistics from the TRMM PR, focusing on shallow storms over the tropical and subtropical oceans. Histograms of storm height are used to map regions where shallow storms are dominant and to determine the modal height of the distribution. In regions of significant rainfall bimodal distributions are found, with the height of the lowest mode making a smooth transition upward from arid to wet regions. Geographic patterns of the low-mode height are mapped for El Niño and La Niña conditions. Statistical models are used to estimate the contribution of shallow storms to rainfall occurrence and to rainfall depth.

Our objectives are to

- derive geographic patterns of shallow storm heights and their seasonal and interannual variability from storm height histogram data;
- develop a parameterization of rainfall rate based on storm height in regions dominated by shallow storms;
- estimate the contribution of precipitation from shallow storms to total precipitation during El Niño and La Niña conditions.

In section 2 the PR and a standard TRMM PR monthly product are described. Section 3 presents a comparison of storm height properties over land and ocean, including storm height distributions over regions with substantial precipitation. Geographical patterns of the low mode are derived via statistical analyses of storm height histograms and are presented in section 4. In section 5 a further statistical analysis of low-mode properties is used to estimate the contribution of shallow storms to total rainfall. Section 6 includes a discussion of radar characteristics that may bias storm height retrievals.

2. Data

The data utilized in this study were derived from TRMM PR observations by the TRMM Science Data Information System (TSDIS). Version 4 PR algorithms provided by the TRMM Science Team were used by TSDIS to derive storm height and rainfall characteristics. The PR, a meteorological radar operating at 13.98 GHz, scans cross-track $\pm 17°$, having 49 fields of view with a horizontal resolution of 4.3 km at nadir and a vertical resolution of 250 m (Kummerow et al. 1998). The sensitivity of the radar is 18 dBZ, sufficient to provide unambiguous detection of rain intensities greater than about 0.5 mm h^{-1}. Product 3A25, denoting monthly averages, is the primary source of data for this study. The monthly product is produced at two resolutions, $5° \times 5°$ and $0.5° \times 0.5°$ latitude–longitude grid cells, from level-2 products, where the level-2 products represent instantaneous PR observations. The level-3 product also includes histogram data, preserving information at the native resolution of the radar, composited within the $5° \times 5°$ grid cells. The histogram data has proven especially useful in the present study. The volume of the level-3 product is 40 megabytes $month^{-1}$, compared to 2 gigabytes day^{-1} for the level-2 product, making the level-3 product ideal for the exploratory analysis presented here.

In the standard processing of level-2 PR data, each profile of radar reflectivity is evaluated for surface detection and rain/hydrometeor detection. When at least three consecutive range bins (750 m) are determined to contain statistically significant hydrometeor echoes, the highest range bin is flagged and a ''storm height'' (product 3A25 terminology) is determined by the height above the standard geoid. The term storm height is also used here to describe deep and shallow PR echoes. Over land, storm heights are not corrected for topography. Storms are classified as convective or stratiform by a horizontal/vertical texture algorithm (a small fraction of ambiguous storm structures are classified as ''other''). Storm height histograms are constructed for each $5° \times 5°$ grid cell for all storms and for convective and stratiform storms separately. Counts of storm heights are recorded in 30 intervals having vertical resolutions of 0.5 km from the surface to 13 km, increasing to 1 km from 13 km to 16 km, ending with a final 4-km bin covering the interval from 16 to 20 km.

Rainfall rates are reported at standard levels of 2, 4, 6, 10, and 15 km in the 3A25 product. In addition a rainfall estimate is made for the PR observation that is closest to the surface, without being contaminated by surface effects. The altitude of this near-surface rainfall

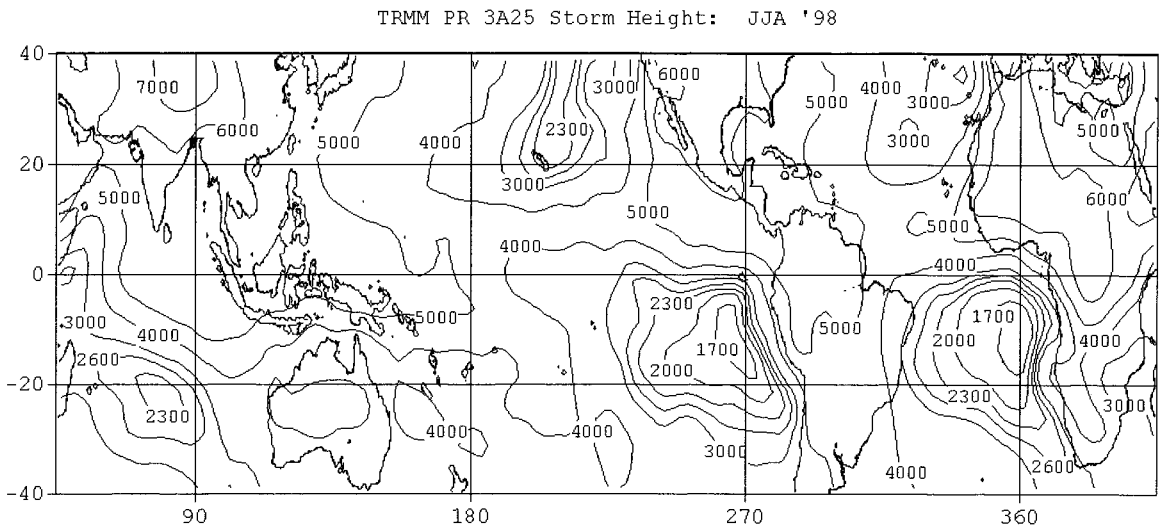

FIG. 1. Average storm height from TRMM standard product 3A25 for JJA98. Units are meters with contours at 17, 20, 23, 26, 30, 40, 50, 60, and 70, $\times 10^2$ m.

rate varies from a few hundred meters at nadir to 2 km at the edge of the scan, due to interactions between the edge of the radar beam and the surface in off-nadir positions. A detailed analysis of the interaction of the radar beam and its sidelobes with the surface and its effects on the detection of storm heights is presented in section 6. A further classification of ''warm rain'' by the PR algorithm is included and will be commented on briefly as its occurrence is exceedingly rare.

3. Storm height observations

Figure 1 shows a map of mean storm height over the 3-month interval of June–July–August 1998 (JJA98). There are several minima near 2 km over the oceans in regions previously associated with marine stratocumulus clouds. The minima west of North and South America appear to be displaced somewhat westward from the primary stratocumulus/stratus regimes identified in previous studies (e.g., Hartmann and Short 1980). The displacement is due to a mixture of low and high storm heights in grid cells adjacent to the coasts, resulting in a higher average storm height. The highest average storm-top heights over the oceans are in the range of 5–6 km over the Indian Ocean and Maritime Continent regions and over the Caribbean/eastern equatorial Pacific Ocean. Values near between 5 and 6 km are seen over the eastern Atlantic ITCZ region, consistent with Global Atmospheric Research Program (GARP) Atlantic Tropical Experiment (GATE) statistics of the maximum height reached by convective storms (Houze and Cheng 1977). Over land, mean storm heights are in the range of 4–6 km, except for a localized minimum over southeastern Africa and a maximum greater than 7 km over the Tibetan Plateau.

Composite storm height histograms were made separately for land and ocean for two seasons: JJA98 (Figs. 2a,b) and December 1997, January and February 1998 (DJF98, Figs. 2c,d). While all four histograms show a peak near 5 km, Figs. 2a,c show a secondary peak of shallow storm heights near 2 km. Note that the secondary peak is dominated by the stratiform classification. Further analysis of storm height distributions below show that the stratiform classification is prominent even in regions where deep convective systems that generate tropical stratiform rain are virtually nonexistent. This characteristic is unexpected and somewhat puzzling. However, the performance of the standard TRMM PR classification algorithm is considered to be beyond the scope of the present study. The focus here is to determine geographical patterns of shallow storms, regardless of classification, over the tropical oceans and to estimate their contribution to total rainfall.

In order to identify geographic regions where shallow storm heights commonly occur, storm height histograms were analyzed for each $5° \times 5°$ grid cell to determine the percentage of storm heights less than 3 km. Figure 3 shows contours of the percent of storm heights lower than 3 km for JJA98. Four maxima exceeding 85% are found in the Atlantic, Pacific, and Indian Oceans in regions previously associated with shallow marine stratocumulus clouds. This special subset of data (including a similar subset from DJF98, not shown) will be utilized in later sections for developing a parameterization of rainfall intensity for shallow storms. It should be noted that only about 1.1% of the PR observations in these regions were associated with precipitation and that only about 5% of the 1.1% were classified as warm rain by the PR algorithm. This strongly suggests that the PR algorithm is underrepresenting warm rain, because the freezing level in these regions is usually greater than 3 km and storm tops are less than 3 km 85% of the time.

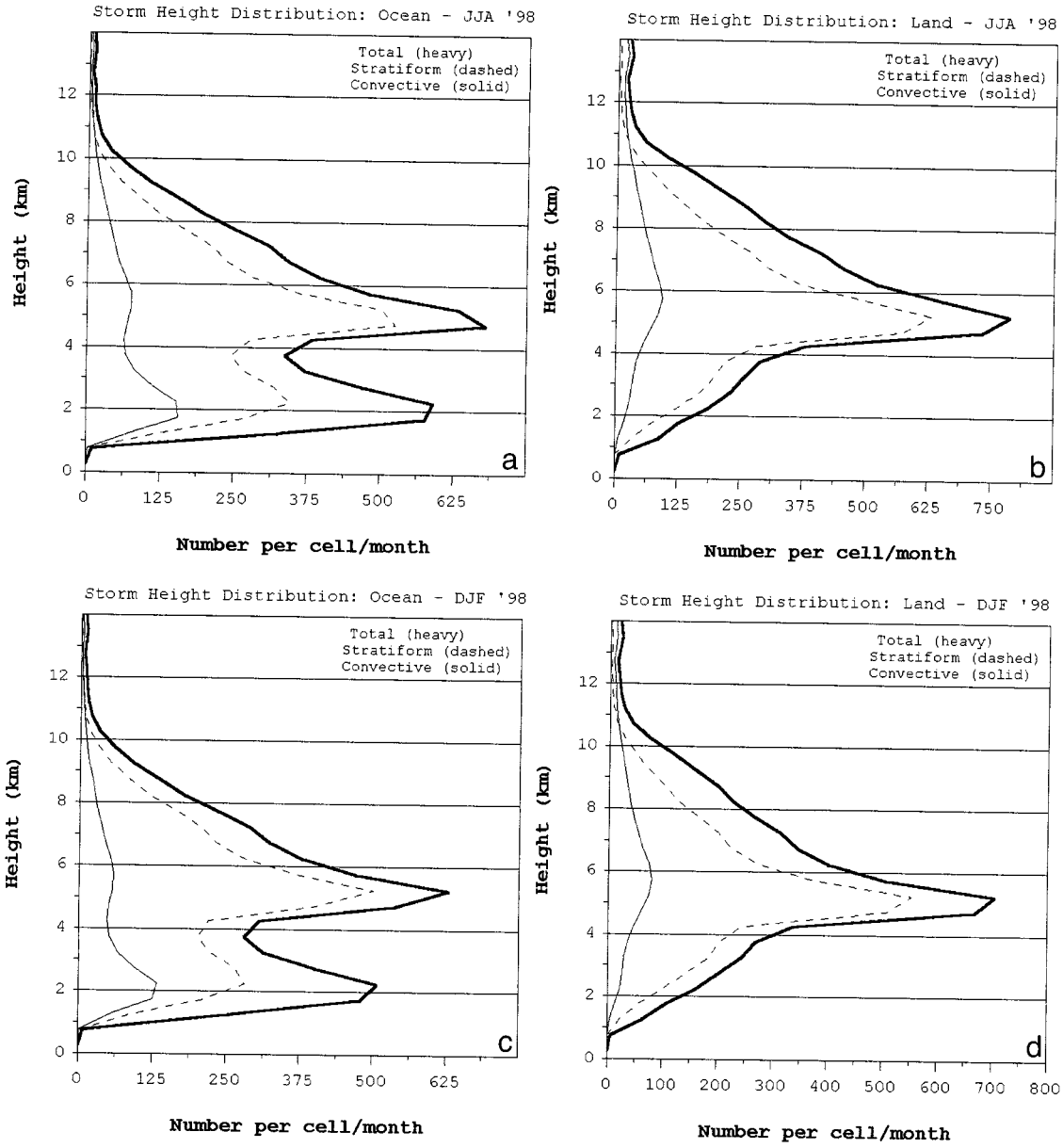

FIG. 2. Composite storm height distribution from 30°N to 30°S for (a) ocean, JJA98; (b) land, JJA98; (c) ocean, DJF98; and (d) land, DJF98. El Niño conditions prevailed during the DJF98 interval, whereas La Niña conditions prevailed during the JJA98 interval.

The warm rain classification was found to be exceedingly rare and will not be commented on further, except briefly in section 6.

Figure 4 shows the percentage of PR profiles with storm heights for JJA98. Figure 4 closely resembles the probability of near-surface rainfall occurrence because more than 95% of storm height retrievals are associated with near-surface rainfall. The contours also resemble seasonal average rainfall patterns (e.g., Xie and Arkin 1997) because temporally and spatially integrated rainfall totals are highly correlated with the probability of rain occurrence (Kedem et al. 1990; Short et al. 1993). The simplest types of rainfall estimation algorithms first make an estimate of rainfall probability and then multiply by a conditional mean rainfall rate to get the total rainfall (Arkin and Meisner 1987). In section 5 this type of algorithm is extended to include storm height information for estimating the total rainfall by shallow storms.

Figure 5a shows composite storm height distributions over the oceans conditioned on >85% of storm-top heights being less than 3 km. There is a sharp maximum just below 2 km and very few storm heights above 4 km. Note also that there are an equal number of con-

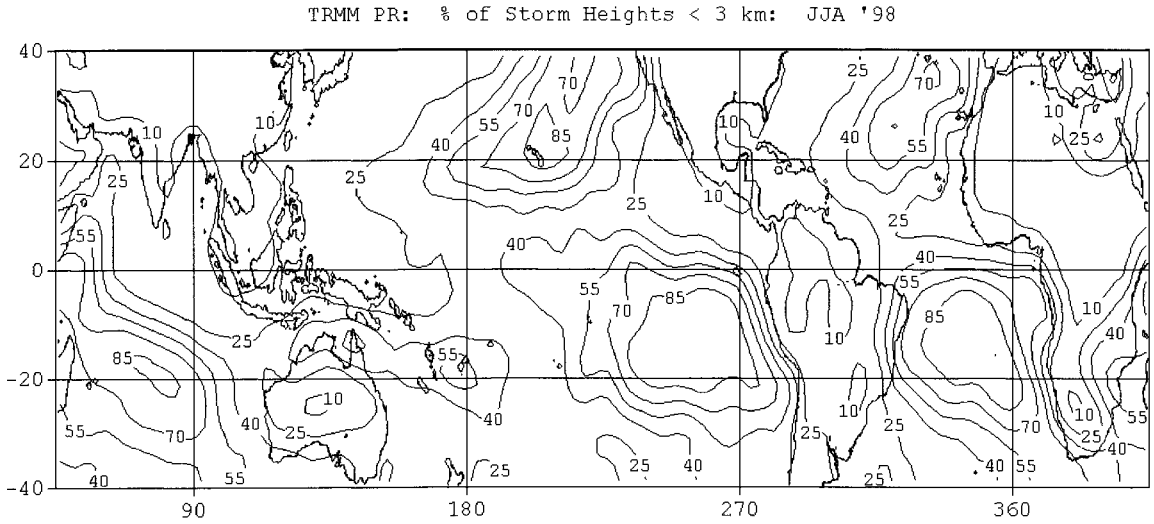

FIG. 3. Percentage of storm heights less than 3 km for JJA98.

vective and stratiform classifications. This again is somewhat puzzling and considered to be a characteristic of the PR storm classification algorithm, requiring further, independent study.

Table 1 indicates that the average monthly rainfall for Fig. 5a was 9.7 mm, with a probability of occurrence of 1.1%. These results are consistent with Soong and Ogura's (1976) diagnosis of undisturbed trade wind conditions over the western Caribbean Sea. They found that the large-scale heat and moisture budgets derived from atmospheric sounding data were consistent with a precipitation rate of 0.29 mm day^{-1} (8.9 mm month^{-1}) being produced by a cumulus cloud population that included precipitating elements with tops at 2 km and a coverage (probability of occurrence) of 0.675%.

Figures 5b,c,d,e,f show storm distributions over the oceans, conditioned on monthly averaged precipitation totals, where Fig. 5b 20–40 mm month^{-1}, Fig. 5e 40–80 mm month^{-1}, Fig. 5d 80–160 mm month^{-1}, Fig. 5e 160–320 mm month^{-1}, and Fig. 5f >320 mm month^{-1}. Table 1 lists the number of grid cells, average rainfall, probability of rain, and height of the low mode for each category. The low-mode height was determined by a quadratic fit to the three lowest points defining a local maximum.

The distributions shown in Figs. 5b–f are distinctly bimodal with a minimum near 3.5 km, suggestive of the 600–800-mb minimum in tropical cloudiness identified by Zuidema (1998). A weak indication of a bimodal storm height distribution was also indicated in GATE

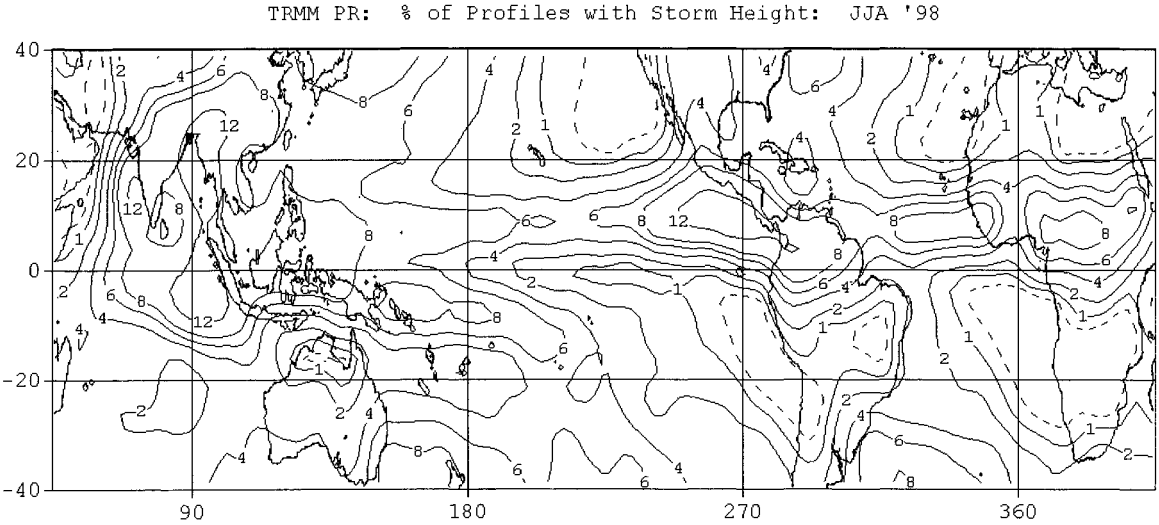

FIG. 4. Percentage of profiles from the TRMM PR with an assigned storm height for JJA98. Contours are at 0.5 (dashed), 1%, 2%, 4%, 6%, 8%, and 12%.

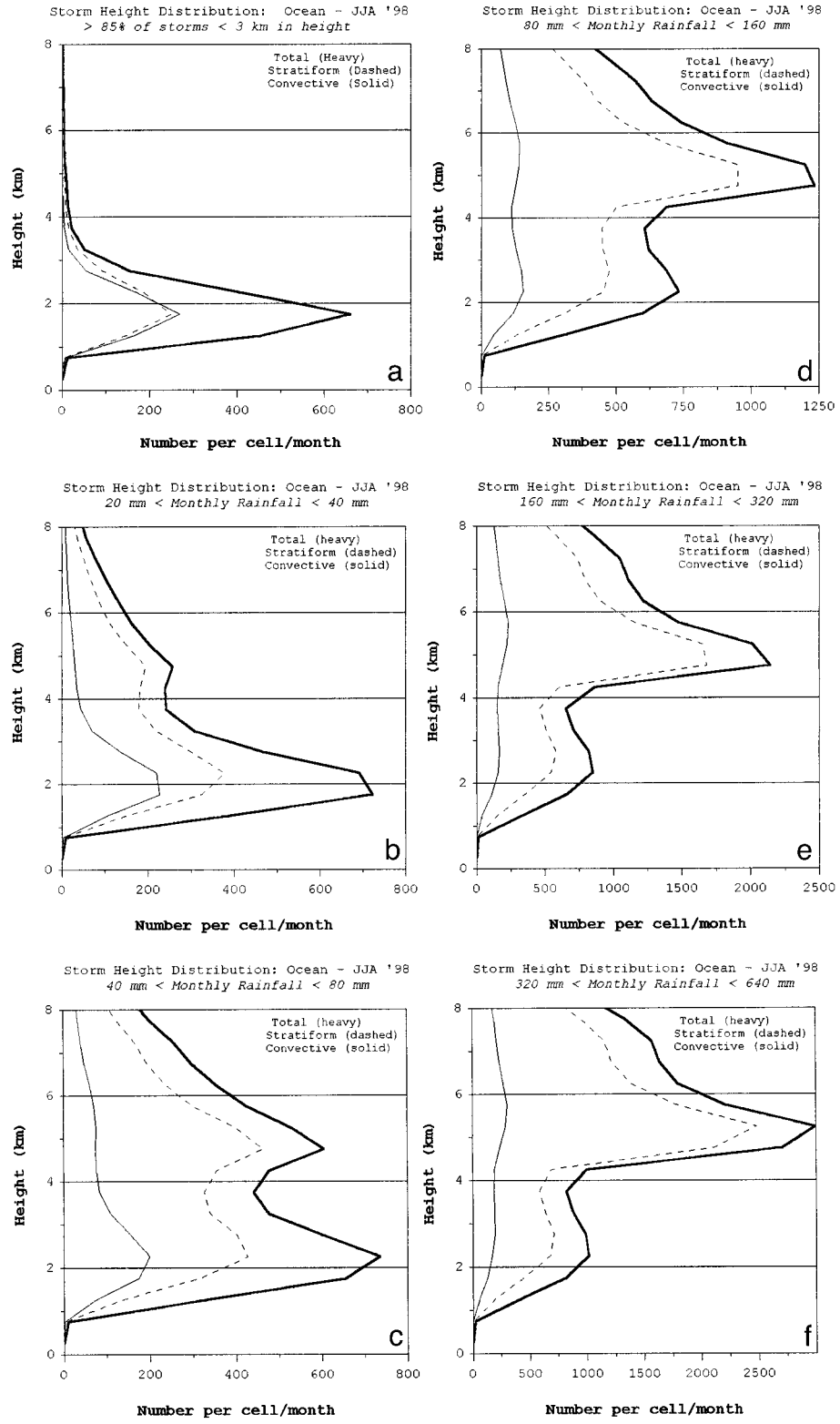

FIG. 5. Composite storm height distributions for JJA98 over the oceans for 5° × 5° grid cells having (a) >85% of storm heights lower than 3 km, (b) 20 mm > monthly rainfall > 40 mm, (c) 40 mm > monthly rainfall > 80 mm, (d) 80 mm > monthly rainfall > 160 mm, (e) 160 mm > monthly rainfall > 320 mm, and (f) 320 mm > monthly rainfall > 640 mm.

TABLE 1. Ocean rainfall statistics for JJA98.

Interval (mm month^{-1})	N (grid cells)	Average rainfall (mm month^{-1})	Probability of rain (%)	Low-mode height (km)
Fig. 5a	69	9.7	1.1	1.72
0–20	210	8.2	0.88	
20–40	97	29.8	2.3	1.95
40–80	122	60.2	3.7	2.19
80–160	119	114	6.2	2.36
160–320	71	209	10.3	2.41
320–640	6	369	13.8	2.44
Summary	625 grid cells	68.1 mm month^{-1}	3.85%	

(Houze and Cheng 1977; Fig. 6) and BOMEX (Lopez 1976; Fig. 6). The upper mode in Figs. 5b–f is consistently near 5 km, close to the average height of the 0°C isotherm in the Tropics, suggesting the influence of the melting level on storm height statistics. A common feature in radar profiles of precipitating clouds is the radar bright band, a region of enhanced reflectivity just below the melting level. It is caused by partially melted ice/snow aggregates whose radar cross section is significantly larger than the dry ice/snow particles above and the completely melted raindrops below (Austin and Bemis 1950). The large difference in the complex index of refraction between water and ice (a factor of 7 dBZ) and in the fall speed of ice aggregates versus raindrops also contributes to the enhanced reflectivity. Given the PR minimum sensitivity of around 18 dBZ (0.5 mm h^{-1}), there appears to be a large number of cases where the brightband enhancement is just detectable by the radar. Weaker returns from ice/snow in the upper part of the storm, which may vary depending on storm strength, are apparently not detectable by the radar, resulting in a maximum occurrence of storm height in association with the radar bright band.

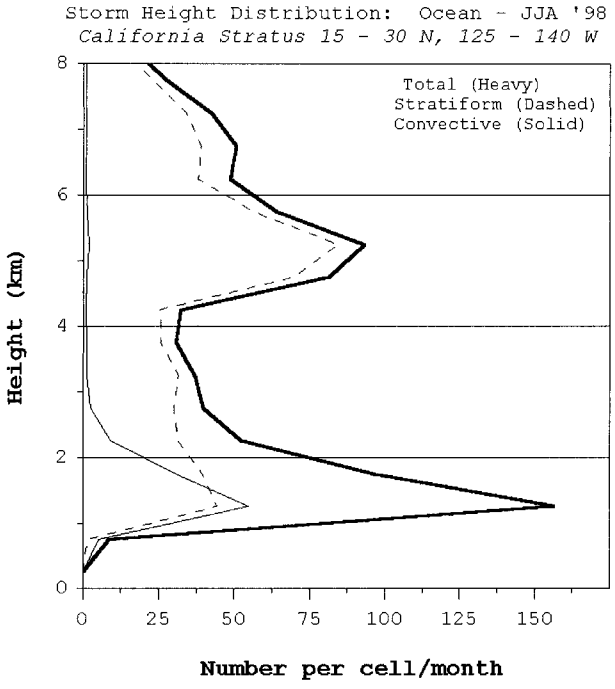

FIG. 6. Composite storm height histogram over the eastern North Pacific Ocean for the domain bounded by 15°–30°N and 140°–125°W. The maximum occurrence is in the height interval from 1000 to 1500 m. A quadratic fit to the peak and points just above and below gives a maximum at 1357 m.

Returning to the low mode observed in Fig. 5a it is quite reasonable to assume that the storm heights are limited by the trade wind inversion, based on the geographical distribution of the data (Fig. 3). This is confirmed in Fig. 6 showing a composite storm height histogram for the northeast Pacific Ocean for JJA98. The region coincides with the FIRE study region of Betts et al. (1992), where the height of low cloud tops was retrieved by a visible/infrared satellite algorithm (Minnis et al. 1987). The retrieval gave a mean height of 1691 m for the July average (1983–87), whereas the JJA98 TRMM PR storm height shows a maximum occurrence between 1250 and 1500 m. Storm-top estimates from the PR would be expected to be lower than cloud-top estimates from visible/infrared instruments, due to the radar's lack of sensitivity to cloud droplets.

However, it is also reasonable to exercise some caution in the interpretation of the low mode appearing in Figs. 5b–f, especially considering the limited sensitivity of the PR to very light rain and clouds. Vigorous trade wind cumuli have been observed to penetrate the trade wind inversion, thus in a pure trade cumulus regime the PR storm height distribution would represent an ensemble of the storms sufficiently active to be detectable by the radar. On the other hand, in the presence of deep convective activity and its accompanying stratiform precipitation, it is possible that widespread layers of weak, decaying stratiform precipitation could produce a large population of low storm heights. These situations could be determined by an examination of the data from visible, infrared, and microwave sensors in combination with the PR data (product 2A25). It is also possible that storms with intermediate heights may occur preferentially in the near proximity of deeper storms, such that the 4.3-km field of view (FOV) of the PR essentially filters out the intermediate storms (DeMott 1999, per-

sonal communication). In addition, the storm height retrieval algorithm is susceptible to errors caused by antenna sidelobes, in the height range from 1.5 to 4 km (see section 6 for a detailed discussion). Nevertheless, the systematic increase in the height and amplitude of the low mode as rainfall increases and the distinct land–sea asymmetry (Fig. 2) warrants further investigation of the phenomenon.

The amplitude of the low mode in Fig. 5 increases slowly (700–1000) as rainfall increases (Figs. 5b–f), whereas the amplitude of the upper mode increases by a factor of 10, and the rainfall increases by a factor of 20. It is evident that the increase in rainfall is primarily due to an increase in deep storms, consistent with previous studies (e.g., Liu et al. 1995; DeMott and Rutledge 1998; Rickenbach and Rutledge 1998). The simplest estimate of the contribution of shallow storm rainfall to total rainfall can be made by assuming it is determined by the rainfall for the unimodal distribution shown in Fig. 5a (9.7 mm month^{-1}), and is constant over the oceans. This results in 14% of the total ocean rainfall for JJA98 (68.1 mm month^{-1}), calculated from a weighted sum of the values in Table 1. However, as an example, consider Fig. 5e and its entry in Table 1 (monthly rainfall 209 mm). The same estimate would indicate shallow storms contributing less than 5% of the total in regions of significant rainfall. Clearly, it is the large areal coverage of the shallow regime that accounts for its nonnegligible contribution to the global average. In the following sections a more comprehensive method will be used, utilizing estimates of the fractional occurrence of shallow storms and an observed correlation between the low-mode height and conditional mean rainfall rate.

4. Analysis of low mode

The presence of the lowest mode in Figs. 5a–f is suggestive of the limiting influence of the trade wind inversion on shallow precipitation. Kinematic and thermodynamic properties of the trade wind inversion are well known from ocean weather station observations (Norris 1998a; Klein et al. 1995; Riehl et al. 1951). Near the west coasts of the major continents the inversion height is generally below 1 km, rising to between 1 and 2 km within a few hundred kilometers of the coast (Nieberger 1960). Within this deeper layer overcast stratus/stratocumulus with drizzle (occasionally heavy; Frisch et al. 1995) frequently occurs, although much of it evaporates before reaching the surface. The inversion rises downstream as boundary layer air is advected over warmer surface waters and the stratus/statocumulus regime eventually transitions to a broken stratocumulus regime and finally to a trade wind cumulus regime (Wyant et al. 1997).

It can be expected that heavy drizzle with an intensity greater than 0.6 mm h^{-1} (Tucker 1961) and an equivalent radar reflectivity greater than 18 dBZ_e would be consistently detectable by the PR, based on a Z–R relation for drizzle of $Z = 140R^{1.5}$ (Joss et al. 1970). During the ASTEX field campaign only a few percent of observed drizzle occurrences exceeded the 18 dBZ_e threshold (Frisch et al. 1995), thus the TRMM PR will significantly underestimate the overall occurrence of drizzle. However, there is evidence of isolated cumuli penetrating through stratocumulus clouds in such regions (Wang and Lenschow 1995), and Petty's (1995) finding of ship reports of showery precipitation in regions normally associated with stratocumulus/stratus. Also, Yuter et al. (2000) have recently reported drizzle cells with scales of 2–3 km exceeding 10 dBZ and peak reflectivities exceeding 25 dBZ over the eastern near-equatorial Pacific Ocean. The persistent nature and high-fractional cloud cover of marine stratocumulus cloud (MSC) fields should guarantee a useful sample of these conditions by the TRMM PR.

Statistics of precipitating trade wind cumulus clouds indicate that they are large enough (>1 km diameter; Benner and Curry 1998) to be readily detectable by the PR, although some limitation in the detection of small weak cells is to be expected. The rainwater content of trade cumulus is reported to be up to 1 g m^{-3} in isolated showers and up to 3 g m^{-3} in line showers (Baker 1993). Corresponding radar reflectivity values are 40 dBZ and 47.8 dBZ, based on the convectve Z–M relation of Tokay and Short (1996; $Z = 10\ 100M^{1.62}$), readily detectable by the PR provided the scale of the echoes is a sufficient fraction of the 4.3-km FOV. An estimate of the minimum detectable cell size for these two reflectivity values can be made by assuming cylindrical, homogeneous echoes, a minimum detectable reflectivity of 18 dBZ, and an instrument response function for the PR that is uniform over the 4.3 km FOV. Under these ideal conditions a 0.34-diameter echo with a reflectivity of 4O dBZ (Z = 10 000) would cover 0.63% of the FOV and have a reflectivity of 18 dBZ (Z = 63). A similar calculation for the 47.8-dBZ threshold results in a minimum detectable cell size of 0.14 km. Shallow trade wind cumuli within enhanced low-level convergence zones upwind of Hawaii have been observed with radar reflectivity values near 60 dBZ (Szumowski et al. 1997), although more typical values indicate the horizontal scale of echoes exceeding 20 dBZ to be 3 km. Modeling and observational studies of enhanced trade wind cumuli indicate strong vertical gradients of liquid water and radar reflectivity near the tops of the clouds (e.g., Rauber et al. 1991; Takahashi 1977; Squires and Warner 1957). Under these conditions the PR storm-top height should closely correspond to the top of the cloud and give some indication of the height of the stable layer that is restricting vertical development.

The presence and height of the low mode in Figs. 5b–f further suggests that regions with increased overall precipitation have a slightly deeper layer of shallow clouds. In order to map properties of the low mode, histograms of storm height were analyzed for every 5° × 5° grid cell over both ocean and land. Storm height

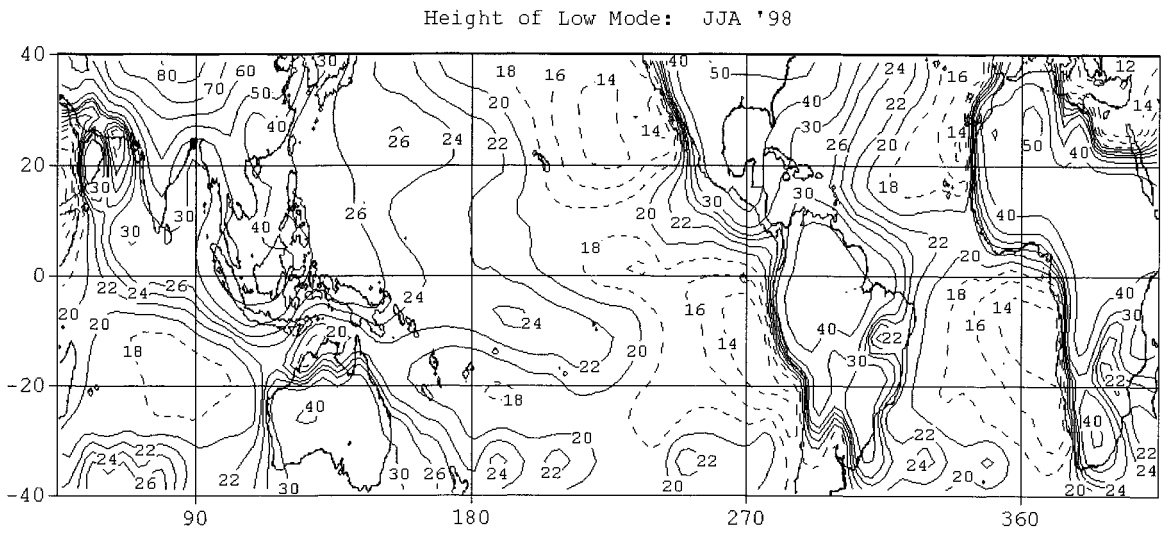

FIG. 7. Lowest mode JJA98. Contours are labeled in hundreds of meters above the standard geoid at 14, 16, 18 (dashed); and 20, 22, 24, 26, 30, 40, 50, 60, 70, and 80 (solid).

histogram were first composited from monthly data for two seasons: DJF98 and JJA98. A weak spatial filter was then applied to each level in the histogram data by forming a weighted average of the storm count in each grid cell with its north–south and east–west neighbors. Weights were 1 for the central grid cell and 0.01 for the surrounding four grid cells. Each histogram was searched for the lowest local maximum, where the maximum and the points just below and above it contained at least 7% of the total points. The 7% threshold was empirically found to eliminate weak, perhaps spurious low-level maxima. A quadratic fit to the three points was made and used to evaluate the height of the local maximum. Out of 614 ocean grid-cell histograms, the heights of 11 maxima were altered by more than 200 m by the weak spatial filter and the 7% criteria for the JJA98 data. The results over land will not be overly emphasized here due to some ambiguity in interpreting the heights that are not corrected for local topography.

Figure 7 shows the height of the lowest mode as determined by the quadratic fitting procedure described above for JJA98. Note that the minima over the eastern Pacific and Atlantic Oceans are now less than 1400 m, and are located close to the west coasts of the continents, consistent with previous studies. The height generally increases westward to near 3000 m over the western oceans, in regions where the probability of storm detection is high (Fig. 4). There is also a clear indication of the SPCZ in Fig. 7 and a minimum in storm heights stretching across northern Australia during its dry season. Southwest of the Indian subcontinent the low-mode height shows a local maximum of 3000 m in the same area identified with an oceanic mini–warm pool (Rao and Sivakumar 1999). A regional maximum greater than 4000 m is located over the Maritime Continent and values greater than 4000 m are also seen over the Gulf of Mexico. The contour patterns of Fig. 7 are in qualitative agreement with previous surveys of the height of the trade wind inversion (see Schubert et al. 1995 and references therein), especially in their depiction of mimima along the west coasts of North and South America and Africa and in the transition to higher values over the ITCZ. This agreement with known climatological features encourages interpretation of the low-mode height as an *index* of the trade inversion height.

Figure 7 also indicates the ITCZs of the eastern Pacific and Atlantic Oceans are associated with relatively shallow low modes, suggestive of advective effects by the NE and SE trades. The ITCZ region southeast of Hawaii was the subject of Janowiak's (1995) comparative study of rainfall estimates based on numerous satellite- and surface-based observations. He concluded that a likely cause for the discrepancies in the estimates was shallow precipitation. In 1997 the PACS/TEPPS field experiment was conducted in the region, finding that the contribution to overall rainfall by small, less organized convection, detected by microwave algorithms but not by infrared cold cloudiness, is key to revealing the true distribution of rainfall in the Pacific (Yuter and Houze 2000). The low-mode height pattern shown in Fig. 7 indicates that the PACS study area is unique, as viewed by the TRMM PR. Further studies of TRMM multisensor data would be helpful in determining the nature of rainfall distributions in this region.

Figure 8 shows the height of the low mode for DJF98: El Niño conditions prevailed over the Pacific Ocean during this time period (Morrissey 1998). Low-mode heights from 2000 to 2400 m are seen across the Pacific on the equator, from the Maritime Continent to South America. The Atlantic ITCZ region is marked by a northward projecting lobe, caused by the rejection of a weak low mode by the 7% criteria mentioned above. A

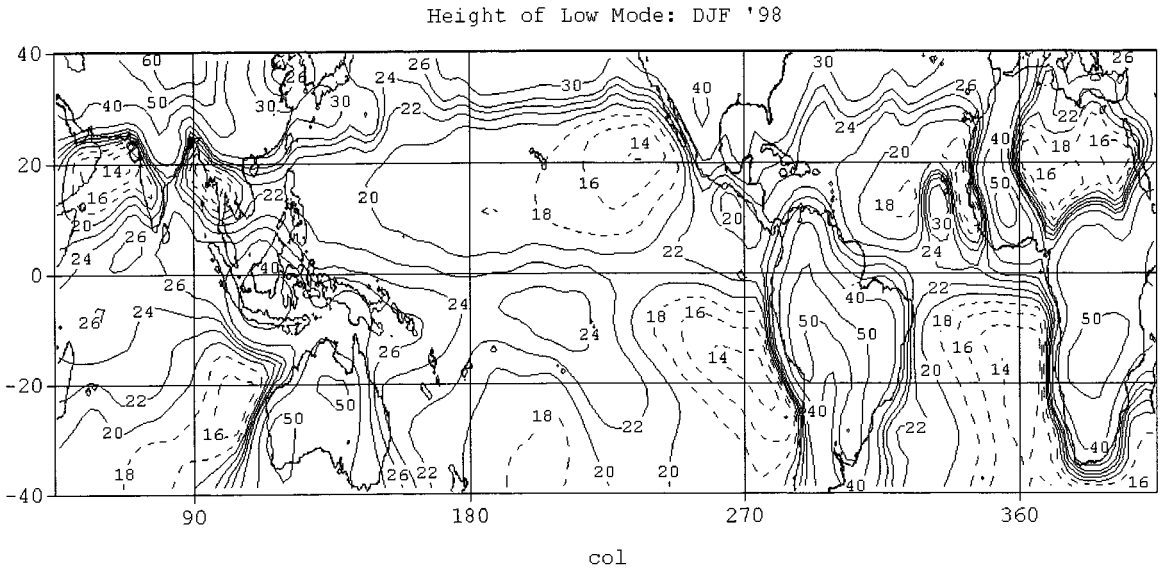

FIG. 8. As in Fig. 7 but for DJF98.

smoother contour pattern would have resulted by accepting the weak low mode in this case. An axis of maximum heights extends across the Indian Ocean, corresponding to the normal position of the ITCZ in that region during northern winter. The regional maximum over the Maritime Continent is south of the island of Borneo and the seas north of Australia show a deeper low mode during their rainy season than during the dry season (Fig. 7).

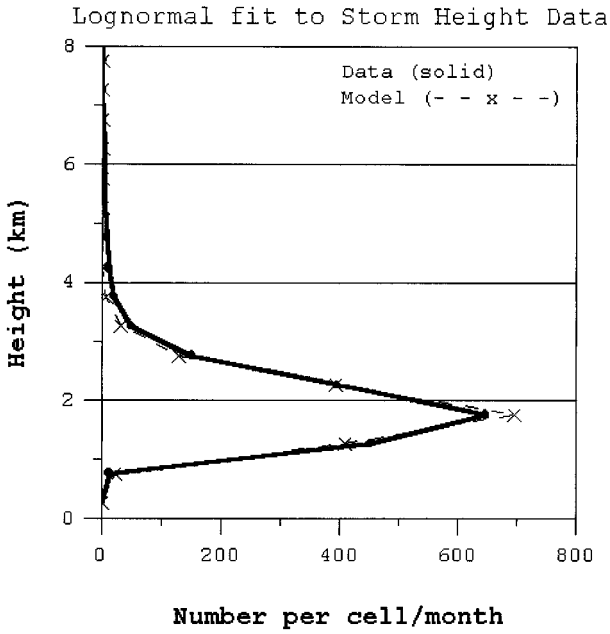

FIG. 9. Lognormal fit to the storm height distribution shown in Fig. 5a.

Lognormal fitting

The lognormal distribution has been used to model numerous properties of precipitation echoes, including height, area, and duration (Lopez 1977; Houze and Cheng 1977). Its general form is described by

$$P(x) = \frac{1}{x\sigma\sqrt{2\pi}} \exp\left[-\frac{1}{2}\left(\frac{\ln x - \mu}{\sigma}\right)^2\right], \qquad (1)$$

with parameters μ and σ. The mode, median, and mean of the distribution are given by exponentiating $\mu - \sigma^2$, μ, and $\mu + \frac{1}{2}\sigma^2$, respectively. The unimodal storm height distribution shown in Fig. 5a is well approximated by a lognormal distribution (Fig. 9), as determined by a minimum χ^2 statistic. Parameter values μ and σ are 0.58 and 0.265, respectively. The mode, median, and mean heights are very close together, being 1.66, 1.79, and 1.85 km, respectively. However, to fit bimodal distributions, such as those seen in Figs. 5b–f, a mixed lognormal distribution would be required.

The objective of the mixed lognormal fitting applied here is to separate bimodal distributions into two parts and to associate a weighting function with each mode. A mixed lognormal distribution requires five parameters to describe a weighted sum of two lognormals:

$$P_{1,2}(x) = gP_1(x) + P_2(x), \qquad (2)$$

with parameters g, σ_1, and μ_1 for the first distribution; and σ_2, μ_2 for the second. Parameters were determined by minimizing a five-dimensional χ^2 statistic. A constraint was added to force the average of the modeled distribution to match the observed average. The fraction of observations associated with the first distribution is $g/(1 + g)$, whereas that associated with the second is $1/(1 + g)$.

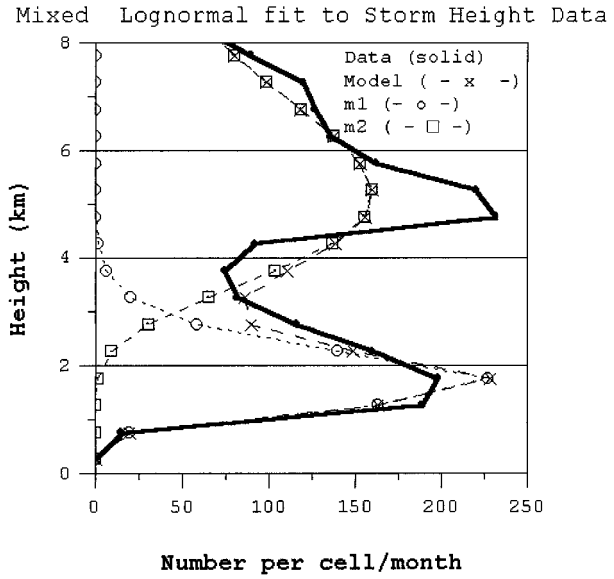

FIG. 10. Mixed lognormal fit to the composite storm height distribution over the northeast Pacific Ocean (10°–40°N, 115°–145°W).

Figure 10 shows the storm height distribution over the northeastern Pacific for JJA98 and a mixed lognormal fit to the data. The parameter values (g, σ_1, μ_1, σ_2, μ_2) are (0.42, 0.58, 0.31, 1.76, 0.35), indicating that 30% of storm heights are associated with the lowest mode. The mode of the lowest (highest) distribution is at 1.62 km (5.14 km). It is clear that the mixed lognormal distribution does not fit the bimodal data as well as the single lognormal distribution fits the unimodal data shown in Fig. 9. Nevertheless, the mixed lognormal fit is useful as an objective method for estimating the fraction of storm heights associated with the lowest mode.

Storm height histograms for each 5° × 5° grid cell were fitted with the mixed lognormal distribution described above by minimizing a χ^2 statistic over the range of heights from 0 to 10 km. The 10-km cutoff was chosen to avoid anomalous high-level storms associated with sidelobe errors (see section 6). Figure 11 shows a map of the percentage of storms associated with the shallow distribution. Geographic patterns over the oceans are similar to those seen in Fig. 3, indicating that the mixed lognormal fit divides the storm height distribution into shallow and deep components in a manner similar to a simple division at a height of 3 km. Notable exceptions occur over land, especially the Tibetan Plateau because the storm height data in product 3A25 are relative to the standard geoid, not local topography.

Figure 12 shows the percentage of storms associated with the shallow distribution for DJF98. The predominantly shallow regimes are in similar positions seen in Fig. 11; however, the maximum near Hawaii is spread across the Pacific Ocean. Also note that the minimum over the central Pacific is located south of the equator and east of the date line, consistent with the location of deep convection during the 1997/98 El Niño event. In both Figs. 11 and 12 values from 20% to 50% are seen over the western Pacific Ocean east of Australia, consistent with Petty's (1999) combined analysis of warm rain using ship observations and satellite infrared data.

5. Rainfall from shallow storms

Storm height statistics found in product 3A25 have been shown to be composed of a mixture of shallow and deep storms. The rainfall statistics must also consist of the same mixture. In order to separate total rainfall into shallow and deep components, a parameterization

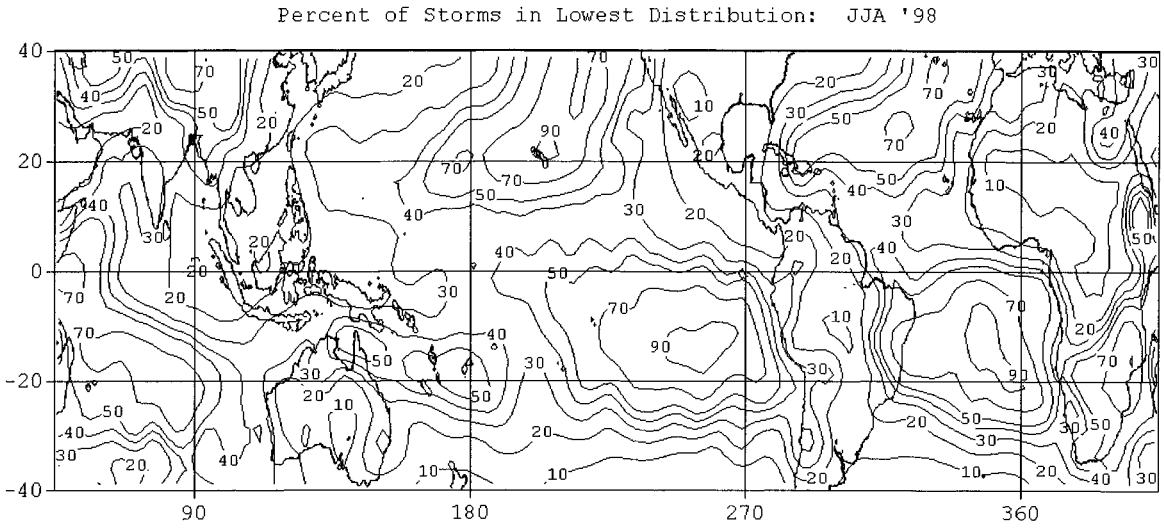

FIG. 11. Percentage of storms associated with the lowest mode for JJA98. Contours are 10%, 20%, 30%, 40%, 50%, 70%, and 90%.

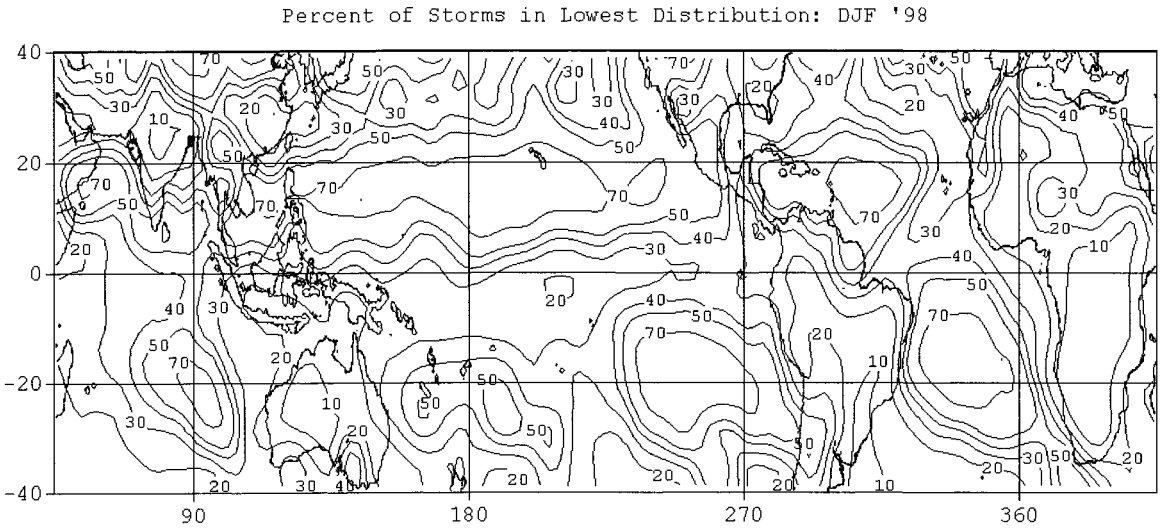

FIG. 12. As in Fig. 11 but for DJF98.

of rainfall rate, based on storm height, is developed below.

The storm height data shown in Fig. 5a was composited from 69 grid cells whose geographic distribution lies inside the 85% contour of Fig. 3. An additional 47 grid cells satisfying this criterion were found during the DJF98 season. They lie over the oceans within the 70% contours shown in Fig. 12. These 116 grid cells represent regions where shallow storms are dominant with the average low-mode height being 1.7 km. The probability of rainfall in these regions is 1.1% (8.2 h month^{-1}), and the conditional mean rainfall rate is 1.2 mm h^{-1}, resulting in an average monthly rainfall of 9.8 mm. The 116 grid cells are found over every major tropical ocean basin, primarily in regions previously associated with trade wind cumulus and in some areas where the marine boundary layer cloudiness transitions from stratocumulus to trade cumulus.

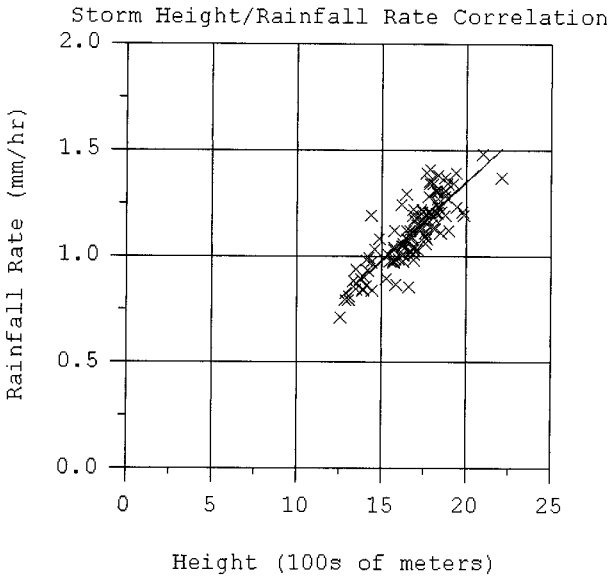

FIG. 13. Average storm height vs conditional rainfall rate for grid cells where >85% of storm heights are lower than 3 km (from JJA98 and DJF98 data). Linear regression gives the relation R_c (mm h^{-1}) = 0.0745(H − 2). The correlation coefficient is 0.71.

Figure 13 shows a scatter diagram of low-mode height versus conditional rainfall rate for the 116 grid cells described above. A linear regression line is also shown (correlation coefficient: 0.71). The linear relationship may be related to that discussed for steady-state stratocumulus cloud depth and drizzle rate (see Austin et al. 1995; Stevens et al. 1998, and references therein), although the cloud depths and rainfall rates in Fig. 13 are somewhat higher. A parameterization of conditional mean rainfall rate based on low-mode height from the regression results in

$$R_c = 0.0745(H - 2), \tag{3}$$

where R_c is conditional mean rainfall rate (mm h^{-1}) and H is low-mode height (hundreds of meters).

The parameterization of rainfall rate based on low-mode height was combined with the percentage of storms in the lowest distribution (Figs. 11 and 12) to estimate shallow precipitation, adopting the following rules. 1) The analysis was restricted to ocean grid cells at latitudes equatorward of ±30°. 2) A low-mode height of less than 3 km must exist in the local storm height histogram, as defined by the 7% criteria in section 4. 3) The percentage of total storms assigned to the shallow category was determined from the gain factor g, of the mixed lognormal fit (Figs. 11 and 12). The equation used to calculate rainfall from shallow storms (R_s) was

$$R_s = P_r P_s R_c T, \tag{4}$$

where P_r is the probability of near-surface rain, P_s is the fraction of storms that are shallow, R_c is the con-

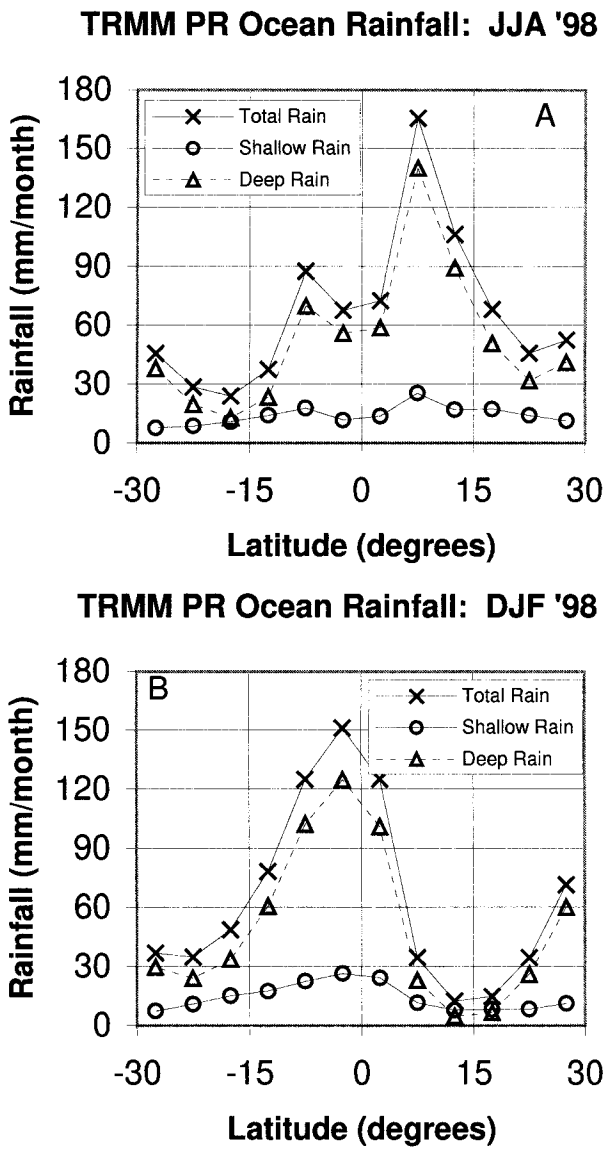

FIG. 14. Zonal averages of total rainfall and rainfall attributed to deep and shallow storms over the oceans for (a) JJA98 and (b) DJF98. Shallow storms account for 21% of the total in JJA98 and 22% in DJF98.

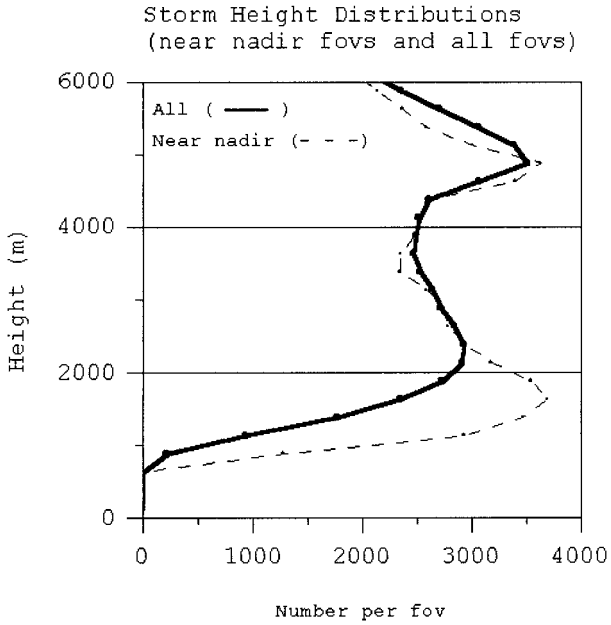

FIG. 15. Ocean storm height distribution derived from all PR 49 FOV (solid) and the inner 7 FOV (dashed) for a 15-day period during Feb 1998.

ditional mean rainfall rate of shallow storms from (3), and T is the number of hours per month. A small percentage of storms do not produce near-surface rainfall. Their effect on the estimation of shallow rainfall is negligible.

Figure 14 shows zonal averages of total rain, shallow rain, and deep rain over the oceans for JJA98. The shallow rain contribution was calculated from (4) and subtracted from total rain to get deep rain. Shallow rain accounts for 21% of the total, as compared to the simple estimate of 14% presented in section 3. The increase is due to the parameterization of conditional rainfall rate as a function of storm depth and the fractional increase in shallow storms as overall rainfall increases. The meridional profile of rainfall shown in Fig. 14a indicates that shallow rain accounts for less than 15% in the zone of maximum rainfall (5°–10°N) and more than 50% in the zone of minimum rainfall (15°–20°S). In Fig. 14b (DJF98) shallow rain accounts for about 22% of total rainfall, with more than 50% contribution in the minimum regions and less than 15% in the maximum. It is interesting to note the consistency of these relative measures in the two seasons, one dominated by the El Niño phenomenon (DJF98) and the other by its opposite, La Niña (JJA98). Apparently the significant variability in the ocean–atmosphere system has little effect on the overall occurrence of shallow rainfall, although geographic patterns may shift dramatically on seasonal and interannual timescales.

6. Discussion and conclusions

a. Mainlobe effects

The PR scans cross-track ±17° from nadir in 0.7° intervals, generating echo profiles at 49 (nadir ±24) beam positions. In the off-nadir positions the edge of the mainlobe intersects the surface while the center is still above the surface. This mainlobe contamination restricts the PR from detecting low-level storms in the off-nadir positions. The maximum effect is realized at the edges of the scan, where storm heights lower than about 2 km cannot be observed. Figure 15 shows composite storm height distributions over the oceans for all 49 FOV and for the inner 7 FOV (nadir ±3) for a 15-

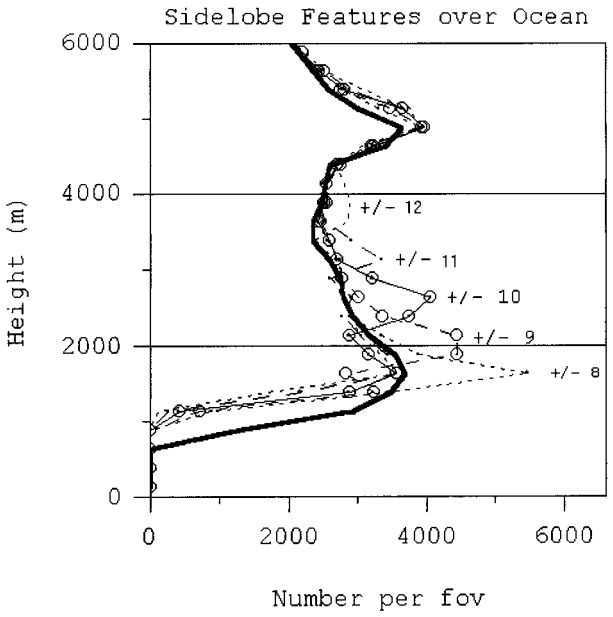

FIG. 16. Sidelobe features detected in storm height statistics of off-nadir FOV. Peaks are shown at beam positions at ±8, 9, 10, 11, and 12, where nadir is beam position 1 and the edge of scan is at beam position ±24.

day period during February 1998. The 49 FOV composite shows a low mode just above 2 km, whereas the inner 7 FOV composite shows a low mode just below 2 km. This result indicates that shallow storms are undersampled by the PR and that a reanalysis of storm height data from near-nadir beam positions would result in a general reduction of the low-mode heights shown in Figs. 7 and 8. It also suggests that the fractional percentage of shallow storms is underestimated in addition to the total rainfall from shallow storms. A rough estimate of these effects can be made by applying the shallow rain estimation algorithm (3) to storm heights below 3-km altitude for the near nadir and full 49 FOV distributions shown in Fig. 15. This results in a 37% increase in the occurrence of shallow storms for the near-nadir sample and a 20% increase in shallow rainfall, but only a 4% increase in total rain (assuming 20% initially for shallow) and a 3% increase in the percentage of rainfall allotted to the shallow category. The effects are not major because the parameterization developed in section 4 assigns lower rainfall rates to the undersampled shallow storms.

b. Sidelobe effects

Figure 16 shows composite storm height distributions from the inner seven FOVs (same as Fig. 15 but solid instead of dashed line) and from pairs of FOVs located at nadir ±8, 9, 10, 11, and 12 beam positions. Anomalous maxima are seen rising in height from 1.75 to 3.75 km as the radar beam scans outward. These maxima are consistent with contamination by the radar sidelobes. When the radar is illuminating a highly reflective surface, such as a calm sea, in an off-nadir beam position, the reflection from a sidelobe may be strong enough to produce an echo that is identified as meteorologically significant. The range to the target is the satellite altitude; however, the target is interpreted as being located along the main beam axis. As a result the target is determined to be above the surface at an altitude that increases as the scan angle increases. Contamination from the sidelobes can produce serious local effects. However, their effects on the present analysis are considered to be minor for three reasons. 1) Shallow heights (<3 km) are affected by 10 beam positions (20% of the total). 2) Globally, the anomalous storm heights appear to increase the observed storm height sample at those beam positions by about 40%. Thus, the overall effect would appear to be an 8% increase in the occurrence of shallow storms. On the basis of the analysis in section 6a above, it would appear that sidelobe contamination might increase the shallow rainfall estimates by less than 2%. 3) The geographical patterns of low-mode heights shown in Figs. 7 and 8 indicate smooth variations associated with well-known climatological features. If sidelobe contamination were seriously affecting storm height information regionally, it would be expected to appear as random maxima at the heights indicated in Fig. 16. Nevertheless, the issue of sidelobe contamination is one that should not be ignored, especially in regions where the probability of real rainfall is low, and the probability of highly reflective surfaces is high.

c. Conclusions

Storm height data from the TRMM PR indicates that bimodal storm height distributions are observed over the oceans, even in regions of significant rainfall, with a shallow mode in the range of 2–3 km and an upper mode near 5 km. The amplitude of the upper mode increases significantly as rainfall increases, indicating that deep storms are largely responsible for the increase in rainfall. The amplitude of the shallow mode is less variable, suggesting a near-constant background of shallow rain over the tropical oceans, even in regions dominated by deep convection. A parameterization of conditional rainfall rate based on storm height is combined with a mixed lognormal fit to storm height histograms to estimate that shallow storms contribute 21% of total rainfall over the tropical oceans during El Niño conditions (DJF98) and 22% during La Niña conditions (JJA98). However, in regions of significant rainfall, shallow storms contribute only about 5% of the total.

Unimodal storm height distributions are found over the oceans in regions previously associated with marine stratocumulus and trade wind cumulus with a modal height near 1.75 km. In these regions the conditional rainfall rate increases linearly with storm height, the monthly average rainfall is 9.7 mm, and shallow storms are detected 1.1% of the time. Of that 1.1% only about

1/20 are classified as ''warm rain'' by the PR algorithm. This strongly suggests that ''warm rain'' is underrepresented by the PR algorithm because the freezing level in these regions is usually greater than 3 km.

Geographical patterns of the height of the low mode make a smooth transition from regions associated with large-scale subsidence to regions associated with low-level convergence and significant rainfall. The patterns are suggestive of the influence of the trade wind inversion in limiting the vertical development of precipitating marine boundary layer clouds over most of the tropical oceans. The height of the low mode is speculatively interpreted as an *index* of the inversion height.

This exploratory analysis of a standard monthly TRMM PR product was complemented by a limited analysis of the 2A25 data, which indicates that shallow storms are undersampled by the PR due to surface clutter from the mainlobe. The undersampling results in an overestimate in the height of the low mode by several hundred meters. The global effect of the undersampling on the rainfall estimate is approximately 3%, although regionally the effect could be as large as 20% in regions where shallow precipitation dominates. Sidelobe contamination was found to have a minor effect on the global storm height distribution, although regional effects are likely to be significant, especially in regions where the probability of rain is low and the probability of highly reflective surfaces is high. Improved storm height detection algorithms can be expected to significantly reduce effects of sidelobe contamination in the products generated in future reprocessing cycles.

Future analysis of TRMM observations of shallow precipitation would benefit by a joint analysis of PR data with observations from the visible, infrared, and microwave sensors on board the observatory. This would allow identification of cloud-top parameters (warm/cold, water/ice, cloud particle size) in addition to characterization of the mesoscale environment (closed/open cell, lines, proximity of deep convection). An analysis of near-nadir data would be helpful to clarify the effects of undersampling on regional estimates of shallow rain, especially in regions where deep convection is rare.

Acknowledgments. The support of Nagoya University and the Institute for Hydrospheric-Atmospheric Sciences to one author (DAS) via a Visiting Research Fellowship is gratefully acknowledged. Dr. J. Awaka and Toshio Iguchi provided valuable insight into the performance characteristics of PR algorithms. Dr. J. Kwiatkowski kindly provided the special PR storm product analyzed in section 6. Prof. B. Kedem generously provided the historic reference to Prof. E. Loomis' work. Special thanks go to Prof. T. N. Krishnamurti for his insight and encouragement regarding this effort.

REFERENCES

Agee, E., and K. E. Dowell, 1974: Observational studies of mesoscale cellular convection. *J. Appl. Meteor.,* **13,** 46–53.

——, T. S. Chen, and K. E. Dowell, 1973: A review of mesoscale cellular convection. *Bull. Amer. Meteor. Soc.,* **54,** 1004–1012.

Albrecht, B. A., C. S. Bretherton, D. Johnson, W. H. Schubert, and A. S. Frisch, 1995: The Atlantic Stratocumulus Transition Experiment. *Bull. Amer. Meteor. Soc.,* **76,** 889–904.

Arkin, P. A., and B. N. Meisner, 1987: The relationship between large-scale convective rainfall and cold cloud over the Western Hemisphere during 1982–84. *Mon. Wea. Rev.,* **115,** 51–74.

Austin, P. M., and A. C. Bemis, 1950: A quantitative study of the ''bright band'' in radar precipitation echoes. *J. Meteor.,* **7,** 145–151.

——, Y. Wang, R. Pincus, and V. Kujala, 1995: Precipitation in stratocumulus clouds: Observational and modeling results. *J. Atmos. Sci.,* **52,** 2329–2352.

——, R. M. Rauber, H. T. Ochs III, and L. J. Miller, 1996: Tradewind clouds and Hawaiian rainbands. *Mon. Wea. Rev.,* **124,** 2126–2151.

Bajuk, L. J., and C. B. Leovy, 1998a: Are there real interdecadal variations in marine low clouds? *J. Climate,* **11,** 2910–2921.

——, and ——, 1998b: Seasonal and interannual variations in stratiform and convective clouds over the tropical Pacific and Indian Oceans from ship observations. *J. Climate,* **11,** 2922–2941.

Baker, M., 1993: Trade cumulus observations. *The Representation of Cumulus Convection in Numerical Models, Meteor. Monogr.,* No. 46, Amer. Meteor. Soc., 29–37.

Benner, T. C., and J. A. Curry, 1998: Characteristics of small tropical cumulus clouds and their impact on the environment. *J. Geophys. Res.,* **103,** 28 753–28 767.

Betts, A. K., P. Minnis, W. Ridgway, and D. F. Young, 1992: Integration of satellite and surface data using a radiative–convective oceanic boundary-layer model. *J. Appl. Meteor.,* **31,** 340–350.

Bretherton, C. S., P. Austin, and S. T. Siems, 1995: Cloudiness and marine boundary layer dynamics in the ASTEX Lagrangian experiments. Part II: Cloudiness, drizzle, surface fluxes, and entrainment. *J. Atmos. Sci.,* **52,** 2724–2735.

Cox, S. K., D. S. McDougal, D. A. Randall, and R. A. Schiffer, 1987: FIRE—The First ISCCP Regional Experiment. *Bull. Amer. Meteor. Soc.,* **68,** 114–118.

DeMott, C. A., and S. A. Rutledge, 1998: The vertical structure of TOGA COARE convection. Part I: Radar echo distributions. *J. Atmos. Sci.,* **55,** 2730–2747.

Firestone, J. K., and B. A. Albrecht, 1986: The structure of the atmospheric boundary layer in the central equatorial Pacific during January and February of FGGE. *Mon. Wea. Rev.,* **114,** 2219–2230.

Frisch, A. S., C. W. Fairall, and J. B. Snider, 1995: Measurement of stratus cloud and drizzle parameters in ASTEX with a K_a-band Doppler radar and a microwave radiometer. *J. Atmos. Sci.,* **52,** 2788–2799.

Gage, K. S., C. R. Williams, and W. L. Ecklund, 1996: Application of the 915-MHz profiler for diagnosing and classifying tropical precipitating cloud systems. *Meteor. Atmos. Phys.,* **59,** 141–151.

Han, Q., W. B. Rossow, and A. A. Lacis, 1994: Near-global survey of effective droplet radii in liquid water clouds using ISCCP data. *J. Climate,* **7,** 465–497.

Hartmann, D. L., and D. A. Short, 1980: On the use of earth radiation budget statistics for studies of clouds and climate. *J. Atmos. Sci.,* **37,** 1233–1250.

Holland, J. Z., and E. M. Rasmussen, 1973: Measurements of the atmospheric mass, energy, and momentum budgets over a 500 km square of tropical ocean. *Mon. Wea. Rev.,* **101,** 856–870.

Houze, R. A., Jr., 1993: *Cloud Dynamics.* International Geophysics Series, Vol. 53, Academic Press, 573 pp.

——, and C.-P. Cheng, 1977: Radar characteristics of tropical convection observed during GATE: Mean properties and trends over the summer season. *Mon. Wea. Rev.,* **105,** 964–980.

Inoue, T., 1987: A cloud type classification with *NOAA-7* split-window measurements. *J. Geophys. Res.,* **92,** 3991–4000.

Janowiak, J. E., P. A. Arkin, P. Xie, M. L. Morrissey, and D. R.

Legates, 1995: An examination of the east Pacific ITCZ rainfall distribution. *J. Climate,* **8,** 2810–2823.
Johnson, R. H., and X. Lin, 1997: Episodic trade wind regimes over the western Pacific warm pool. *J. Atmos. Sci.,* **54,** 2020–2034.
——, P. E. Ciesielski, and K. A. Hart, 1996: Tropical inversions near the 0°C level. *J. Atmos. Sci.,* **53,** 1838–1855.
Joss, J., K. Schran, J. C. Thoms, and A. Waldvogel, 1970: On the quantitative determination of precipitation by radar. Scientific Communication 63, Research Department of the Federal Commission on the Study of Hail Formation and Hail Suppression, Ticinese Observatory of the Swiss Central Meteorological Institute, 38 pp. [Available from Swiss Federal Institute of Technology Zurich, ETH Zortrum, CH-8092 Zurich, Switzerland.]
Kedem, B., L. S. Chiu, and Z. Karni, 1990: An analysis of the threshold method for measuring area-averaged rainfall. *J. Appl. Meteor.,* **29,** 3–20.
Klein, S. A., and D. L. Hartmann, 1993: The seasonal cycle of low stratiform clouds. *J. Climate,* **6,** 1587–1606.
——, ——, and J. R. Norris, 1995: On the relationships among low-cloud structure, sea surface temperature, and atmospheric circulation in the summertime northeast Pacific. *J. Climate,* **8,** 1140–1155.
Kummerow, C., W. S. Olson, and L. Giglio, 1996: A simplified scheme for obtaining precipitation and vertical hydrometeor profiles from passive microwave sensors. *IEEE Trans. Geosci. Remote Sens.,* **34,** 1213–1232.
——, W. Barnes, T. Kozu, J. Shiue, and J. Simpson, 1998: The Tropical Rainfall Measuring Mission (TRMM) sensor package. *J. Atmos. Oceanic Technol.,* **15,** 808–816.
Lavoie, R. L., 1967: The warm rain project in Hawaii. *Tellus,* **19,** 347.
Lin, B., and W. B. Rossow, 1997: Precipitation water path and rainfall rate estimates over oceans using special sensor microwave imager and International Satellite Cloud Climatology Project data. *J. Geophys. Res.,* **102,** 9359–9374.
——, P. Minnis, B. Weilicki, D. R. Doelling, R. Palikonda, D. F. Young, and T. Uttal, 1998: Estimation of water cloud properties from satellite microwave, infrared and visible environments in oceanic environments. Part 2: Results. *J. Geophys. Res.,* **103,** 3887–3905.
Liu, G., J. A. Curry, and R.-S. Sheu, 1995: Classification of clouds over the western equatorial Pacific Ocean using combined infrared and microwave satellite data. *J. Geophys. Res.,* **100,** 13 811–13 826.
Loomis, E., 1882: Contributions to meteorology: Being results derived from an examination of observations of the United States Signal Service and from other sources. *Amer. J. Sci.,* **23,** 1–25.
Lopez, R. E., 1976: Radar characteristics of the cloud populations of tropical disturbances in the northwest Atlantic. *Mon. Wea. Rev.,* **104,** 268–283.
——, 1977: The lognormal distribution and cumulus cloud populations. *Mon. Wea. Rev.,* **105,** 865–872.
Mapes, B. E., and P. Zuidema, 1996: Radiative–dynamical consequences of dry tongues in the tropical troposphere. *J. Atmos. Sci.,* **53,** 620–638.
Merceret, F. J., 1976: Air-borne hot film measurements of the small-scale structure of atmospheric turbulence during GATE. *J. Atmos. Sci.,* **33,** 1739–1746.
Minnis, P., E. F. Harrison, and G. G. Gibson, 1987: Cloud cover over the equatorial eastern Pacific derived from July 1983 ISCCP data using a hybrid bispectral threshold method. *J. Geophys. Res.,* **92,** 4051–4073.
Morrissey, M. L., Ed., 1998: *Pacific ENSO Update.* Vol. 4, No.4, p. 1. [Available from Pacific ENSO Applications Center, University of Hawaii, Department of Meteorology, 2525 Correa Rd., HIG 350, Honolulu, HI 96791.]
Nieburger, M., 1960: The relation of air mass structure to the field of motion over the eastern North Pacific Ocean in summer. *Tellus,* **12,** 31–40.
Norris, J. R., 1998a: Low cloud type over the ocean from surface observations. Part I: Relationship to surface meteorology and the vertical distribution of temperature and moisture. *J. Climate,* **11,** 369–382.
——, 1998b: Low cloud type over the ocean from surface observations: Part II: Geographical and seasonal variations. *J. Climate,* **11,** 383–403.
Petty, G. W., 1994: Physical retrievals of over-ocean rain rate from multi-channel microwave imagery. Part I: Theoretical characteristics of normalized polarization and scattering indices. *Meteor. Atmos. Phys.,* **54,** 79–100.
——, 1995: Frequencies and characteristics of global oceanic precipitation from shipboard present-weather reports. *Bull. Amer. Meteor. Soc.,* **76,** 1593–1616.
——, 1999: Prevalence of precipitation from warm-topped clouds over eastern Asia and the western Pacific. *J. Climate,* **12,** 220–229.
Ramage, C. S., S. J. S. Khalsa, and B. N. Meisner, 1981: The central Pacific near-equatorial convergence zone. *J. Geophys. Res.,* **86,** 6580–6598.
Rao, R. R., and R. Sivakumar, 1999: On the possible mechanisms of the evolution of a mini-warm pool during the pre-summer monsoon season and the genesis of onset vortex in the south-eastern Arabian Sea. *Quart. J. Roy. Meteor. Soc.,* **125,** 787–809.
Rauber, R. A., K. V. Beard, and B. M. Andrews, 1991: A mechanism for giant raindrop formation in warm shallow convective clouds. *J. Atmos. Sci.,* **48,** 1791–1797.
Rickenbach, T. M., and S. A. Rutledge, 1998: Convection in TOGA COARE: Horizontal scale, morphology, and rainfall production. *J. Atmos. Sci.,* **55,** 2715–2729.
Riehl, H., T. C. Yeh, J. S. Malkus, and N. E. La Seur, 1951: The north-east trade of the Pacific Ocean. *Quart. J. Roy. Meteor. Soc.,* **77,** 598–626.
Rossow, W. B., and R. A. Schiffer, 1991: ISCCP cloud data products. *Bull. Amer. Meteor. Soc.,* **72,** 2–20.
Schiffer, R. A., and W. B. Rossow, 1983: The International Satellite Cloud Climatology Project (ISCCP): The first project of the World Climate Research Programme. *Bull. Amer. Meteor. Soc.,* **64,** 779–784.
Schubert, W. H., P. E. Ciesielski, C. Lu, and R. H. Johnson, 1995: Dynamical adjustment of the trade wind inversion layer. *J. Atmos. Sci.,* **52,** 2941–2952.
Short, D. A., K. Shimizu, and B. Kedem, 1993: Optimal thresholds for the estimation of area rain-rate moments by the threshold method. *J. Appl. Meteor.,* **32,** 182–192.
Simpson, J., J. Halverson, H. Pierce, C. Morales, and T. Iguchi, 1998: Eyeing the eye: Exciting early stage science results from TRMM. *Bull. Amer. Meteor. Soc.,* **79,** 1711.
Smolarkiewicz, P. K., R. M. Rasmusson, and T. L. Clark, 1988: On the dynamics of Hawaiian cloud bands: Island forcing. *J. Atmos. Sci.,* **45,** 1872–1905.
Soong, S.-T., and Y. Ogura, 1976: A determination of the trade-wind cumuli population using BOMEX data and an axisymmetric cloud model. *J. Atmos. Sci.,* **33,** 992–1007.
Squires, P., and J. Warner, 1957: Some measurements in the orographic cloud of the island of Hawaii and in trade wind cumuli. *Tellus,* **9,** 475–494.
Stevens, B., W. R. Cotton, G. Feingold, and C.-H. Moeng, 1998: Large-eddy simulations of strongly precipitating, shallow, stratocumulus-topped boundary layers. *J. Atmos. Sci.,* **55,** 3616–3638.
Szumowski, M. J., R. M. Rauber, H. T. Ochs III, and L. J. Miller, 1997: The microphysical structure and evolution of Hawaiian rainband clouds. Part I: Radar observations of rainbands containing high reflectivity cores. *J. Atmos. Sci.,* **54,** 369–385.
Takahashi, T., 1977: A study of Hawaiian warm rain showers based on aircraft observation. *J. Atmos. Sci.,* **34,** 1773–1790.
Thiele, O. W., 1988: Validating space observations of rainfall. *Tropical Rainfall Measurements,* J. S. Theon and N. Fugono, Eds., A. Deepak Publishing, 415–423.
Tokay, A., and D. A. Short, 1996: Evidence from tropical raindrop

spectra of the origin of rain from stratiform versus convective clouds. *J. Appl. Meteor.,* **35,** 355–371.

Tucker, G. B., 1961: Precipitation over the north Atlantic Ocean. *Quart. J. Roy. Meteor. Soc.,* **87,** 147–158.

Wang, Q., and D. H. Lenschow, 1995: An observational study of the role of penetrating cumulus in a marine stratocumulus-topped boundary layer. *J. Atmos. Sci.,* **52,** 2778–2787.

Wang, S., and Q. Wang, 1994: Roles of drizzle in a one-dimensional third-order turbulence closure model of the nocturnal stratus-topped marine boundary layer. *J. Atmos. Sci.,* **51,** 1559–1576.

Warren, S. G., C. J. Hahn, J. London, R. M. Chervin, and R. L. Jenne, 1988: Global distribution of total cloud cover and cloud type amounts over ocean. NCAR Tech. Note NCAR/TN-317+STR, National Center for Atmospheric Research, Boulder, CO, 29 pp + 200 maps.

Webster, P. J., and R. Lukas, 1992: TOGA COARE: The Coupled Ocean–Atmosphere Response Experiment. *Bull. Amer. Meteor. Soc.,* **73,** 1377–1416.

Wilheit, T. T., 1986: Some comments on passive microwave measurement of rain. *Bull. Amer. Meteor. Soc.,* **67,** 1226–1232.

Woodruff, S. D., R. J. Slutz, R. L. Jenne, and P. M. Stuerer, 1987: A Comprehensive Ocean–Atmosphere Data Set. *Bull. Amer. Meteor. Soc.,* **68,** 1239–1250.

Wyant, M. C., C. S. Bretherton, H. A. Rand, and D. E. Stevens, 1997: Numerical simulations and a conceptual model of the stratocumulus to trade cumulus transition. *J. Atmos. Sci.,* **54,** 168–192.

Xie, P., and P. A. Arkin, 1997: Global precipitation: A 17-year monthly analysis based on gauge observations, satellite estimates, and numerical model outputs. *Bull. Amer. Meteor. Soc.,* **78,** 2539–2558.

Yuter, S. E., and R. A. Houze Jr., 2000: The 1997 Pan American Climate Studies Tropical Eastern Pacific Process Study. Part I: ITCZ region. *Bull. Amer. Meteor. Soc.,* **81,** 451–481.

——, Y. L. Serra, and R. A. Houze Jr., 2000: The 1997 Pan American Climate Studies Tropical Eastern Pacific Process Study. Part II: Stratocumulus region. *Bull. Amer. Meteor. Soc.,* **81,** 483–499.

Zuidema, P., 1998: The 600–800-mb minimum in tropical cloudiness observed during TOGA COARE. *J. Atmos. Sci.,* **55,** 2220–2228.